Development and application of a ray-tracing code integrating with 3D equilibrium mapping in LHD ECH experiments

メタデータ	言語: eng
	出版者:
	公開日: 2021-12-23
	キーワード (Ja):
	キーワード (En):
	作成者: Tsujimura, Ii Toru, KUBO, Shin, TAKAHASHI, Hiromi, MAKINO, Ryohei, SEKI, Ryosuke, YOSHIMURA, Yasuo, IGAMI, Hiroe, SHIMOZUMA, Takashi, IDA, Katsumi, SUZUKI, Chihiro, EMOTO, Masahiko, YOKOYAMA, Masayuki, Kobayashi, Tatsuya, Moon, C., NAGAOKA, Ken-ichi, OSAKABE, Masaki, KOBAYASHI, Sakuji, ITO, Satoshi, MIZUNO, Yoshinori, OKADA, Koji, EJIRI, Akira, MUTOH, Takashi, LHD, Experiment Group
	メールアドレス:
	所属:
URL	http://hdl.handle.net/10655/00012830

Development and application of a ray-tracing code integrating with 3D equilibrium mapping in the LHD ECH experiments

T. Ii Tsujimura[1], S. Kubo[1], H. Takahashi[1,2], R. Makino[1], R. Seki[1], Y. Yoshimura[1], H. Igami[1], T. Shimozuma[1], K. Ida[1,2], C. Suzuki[1], M. Emoto[1], M. Yokoyama[1], T. Kobayashi[1,2], C. Moon[1], K. Nagaoka[1,2], M. Osakabe[1,2], S. Kobayashi[1], S. Ito[1], Y. Mizuno[1], K. Okada[1], A. Ejiri[3], T. Mutoh[1,2], and the LHD Experiment Group[1]

[1] National Institute for Fusion Science, Toki 509-5292, Japan

[2] SOKENDAI (The Graduate University for Advanced Studies), Toki 509-5292, Japan

[3] Graduate School of Frontier Sciences, The University of Tokyo, Kashiwa 277-8561, Japan

E-mail: `tsujimura.tohru@nifs.ac.jp`

18 October 2015

Abstract. The central electron temperature has successfully reached up to 7.5 keV in Large Helical Device (LHD) plasmas with a central high-ion temperature of 5 keV and central electron density of 1.3×10^{19} m^{-3}. The result was obtained by heating with a newly-installed 154 GHz gyrotron and also optimization of injection geometry in electron cyclotron heating (ECH). The optimization has been carried out by using the ray-tracing code "*LHDGauss*," which has been upgraded to include the rapid post-processing three-dimensional (3D) equilibrium mapping obtained from experiments. For ray-tracing calculations, *LHDGauss* can automatically read the relevant data registered in the LHD database after a discharge, such as ECH injection settings (e.g., Gaussian beam parameters, target positions, polarization, and ECH power) and Thomson scattering diagnostic data along with the 3D equilibrium mapping data. The equilibrium map of the electron density and temperature profiles is then extrapolated into the region outside of the last closed flux surface. Mode purity, or the ratio between the ordinary mode and the extraordinary mode, is obtained by calculating the 1D full-wave equation along the direction of the rays from the antenna to the absorption target point. Using the virtual magnetic flux surfaces, the effects of the modeled density profiles and the magnetic shear at the peripheral region with a given polarization are taken into account. Power deposition profiles calculated for each Thomson scattering measurement timing are registered in the LHD database. Adjustment of the injection settings for the desired deposition profile from feedback provided on a shot-by-shot basis has resulted in an effective experimental procedure.

1. Introduction

Optimal injection settings of electron cyclotron heating (ECH) are essential for achieving the desired power deposition and reducing the stray radiation level in the vessel. In particular,

realizing on-axis heating can result in a high central electron temperature. Since plasma parameters, such as the profiles of electron temperature T_e and electron density n_e, vary during a plasma discharge [1, 2], optimal injection settings have to be determined and adjusted according to those plasma parameters.

A ray-tracing calculation for the EC wave can predict the power deposition profile from the combination of the magnetic field configuration, ECH injection settings, and T_e and n_e profiles in a plasma equilibrium. A realistic calculation can be performed by taking detailed information into account. In particular, refraction of rays in the peripheral region of helical plasmas such as in the Large Helical Device (LHD) [3], which is the largest heliotron-type superconducting device in the world with the capability of generating numerous 3D equilibria in a variety of heliotron configurations, cannot be neglected due to a finite density gradient. In addition, since strong magnetic shear exists in the region, the polarization of the injected millimeter waves has to be carefully adjusted in order to excite pure ordinary (O) mode or extraordinary (X) mode at the resonance layer. For an effective absorption of high power EC beams, the effects of refraction and pure mode excitation are also important in tokamak plasmas such as ITER or future fusion plasmas.

Precise evaluation of the deposition profile is also essential for the study of transport. For instance, modulation ECH (MECH) has been used to generate heat pulses, which are used to evaluate cross-field electron thermal transport [4, 5, 6]. In such studies, precise identification of deposition profile is quite important.

Recently, a rapid post-processing magnetic coordinate mapping system, or a three-dimensional (3D) equilibrium mapping system, has been developed and applied to LHD experiments [7]. The rapid post-processing equilibrium mapping is based on the selection of a best fit profile among thousands of equilibria pre-calculated with the VMEC code [8]. The Thomson scattering diagnostic system provides the input data for the mapping [9]. As a result, non-axisymmetric 3D equilibrium for every Thomson scattering time slice of every shot is offered rapidly after the shot during LHD experiments. The mapping data can be available after the discharge, i.e., the post-shot analyses to catch up with the experimental sequence of shots. This mapping system is now incorporated into the "*AutoAna*" (auto analyzed data registration to the LHD analyzed data server) system [10], which automatically processes physical raw data obtained from LHD experiments and registers analyzed data such as rapid post-processing 3D equilibrium mapping of all the time slices of the Thomson scattering data during experiments.

Until now, conventional ray-tracing calculations using the ray-tracing code "*LHDGauss*" without the rapid post-processing 3D equilibrium mapping system have been conducted for certain shots to study ECH power deposition [11, 12, 13]. Therefore, feedback of the injection settings to meet the required deposition profile was not available on a shot-by-shot basis during experiments, which often resulted in performing the experiments under an unintended heating condition (e.g., off-axis heating).

This paper reports the upgrade and the outcome of the ray-tracing code *LHDGauss*, which now includes the rapid post-processing 3D equilibrium mapping system as well as the mode purity analyses for calculating absolute values of ECH power deposition. Using this

upgraded *LHDGauss*, we have succeeded in increasing the central electron temperature T_{e0} of a high-ion-temperature T_i plasma, and the high T_e-T_i parameter regime of the LHD plasmas was expanded.

This paper is organized as follows. Section 2 together with Appendix A and Appendix B describes an overview of *LHDGauss*. In section 3, the calculation results and some experimental results are compared. In section 4, the successful results of increased T_e with feedback-tuned ECH injection settings are presented. Section 5 summarizes this paper.

2. Ray-tracing code "LHDGauss"

LHDGauss is one of the multi-ray-tracing codes [14, 15, 16] that calculate ray trajectories by solving the eikonal equation under the WKB approximation and calculate the power absorption along the ray propagation. This code is used to calculate propagation of EC waves from the injection antenna as a Gaussian beam in the LHD vacuum region into the LHD plasma and also to calculate absorption of the waves in the plasma to obtain the power deposition profile. This code is currently dedicated to ECH experiments on the LHD. The ECH system on the LHD is summarized, for example, in references [17, 18, 19]. *LHDGauss* is unique in that the multi-rays are distributed so as to simulate the Gaussian beam adopted in the LHD ECH system, in that the rapid post-processing magnetic coordinate mapping system is adopted, and in that the mode purity, which is the ratio between the ordinary (O) mode and the extraordinary (X) mode, is determined by solving the 1D full-wave equation from the injection antenna to the absorption target point, where the effects of the n_e profile and the magnetic shear at the peripheral region of an LHD plasma under a given polarization are taken into account by using the extrapolated virtual magnetic flux surfaces. The effect of refraction of rays at the peripheral region outside the last closed flux surface (LCFS) with a finite density gradient is also included in this code by use of the modeled density profile with the extrapolated 3D equilibrium mapping.

The outline of the calculation procedure of *LHDGauss* is described in figure 1.

Firstly, input files for ray-tracing calculations are prepared in the calculation server for *LHDGauss*. The processed Thomson scattering diagnostic data, i.e., "*TSMAP*," "*TSMESH*," and "*TSWPE*," are read from the LHD database server [7]. The rapid post-processing equilibrium mapping, based on VMEC equilibria, is applied for the equilibrium within the LCFS in the *LHDGauss* code. *TSMAP* is equilibrium mapping that relates the real coordinate R to the effective minor radius r_{eff} using the T_e and n_e profiles. *TSMESH* also relates the real cylindrical coordinates (R, Z, Φ) to r_{eff} for the LHD. The cylindrical coordinates are then transferred to the Cartesian coordinates (X, Y, Z) for ray-tracing calculations. *TSWPE* fits the T_e and n_e profiles inside the LCFS with polynomial functions in r_{eff}. A Gaussian function is added to a polynomial function to express an electron internal transport barrier with a peaked profile in T_e [21, 22]. Since the $n_e(r_{eff})$ profile is given not only inside the LCFS but also in the peripheral region (outside of the LCFS) to some extent where the Thomson scattering diagnostics are available, the $n_e(r_{eff})$ data outside the LCFS are fitted by exponentially-decaying functions connected continuously with the fitted functions inside
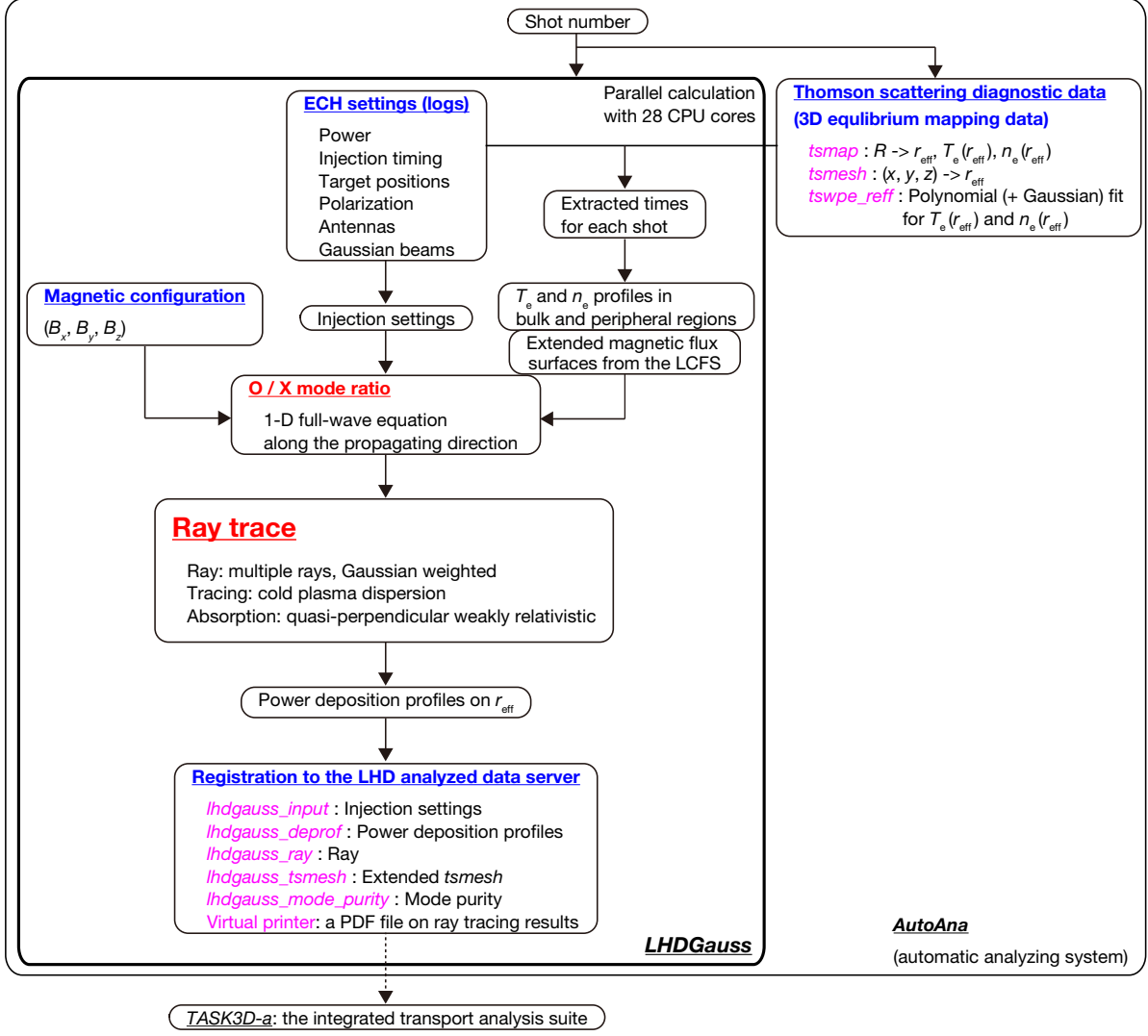
Figure 1. Calculation procedure of the ray-tracing code *LHDGauss*. This code is incorporated into the *AutoAna* system [10]. The output file of power deposition profiles will be included as an input file for the *TASK3D-a* [20].

the LCFS. Then, the 3D equilibrium map is virtually extrapolated far outside of the peripheral region to the first wall of the LHD by using an extrapolation method, which is summarized in Appendix A. Although the n_e profile in this region may not be a flux function, the extrapolated profiles are chosen to be consistent with the Thomson scattering diagnostics available outside the LCFS. It is recognized that the pressure on the magnetic flux surface can be expressed by the flux function in the LHD irrespective of the neighborhood of the diagnostics position or EC-beam launch ports. A possible error regarding the extrapolation process arises from the reduced accuracy of the extrapolated points far from the LCFS due to lack of the points inside the LCFS. However, the error does not affect either polarization or refraction of rays since the electron density at those regions are too low. Thus, the extrapolated 3D equilibrium mapping with the interface region between the plasma region and the vacuum region enables the modeling of the propagation of the EC waves in the entire region from the injection

antenna to the plasma core.

All vacuum magnetic field components on given mesh points for most of the combinations of each magnetic field coil are pre-registered in the *LHDGauss* calculation server, and one of them is referred to before the ray-tracing calculation. Since the 3D equilibrium mapping does not provide the magnetic field information outside the LCFS, the vacuum magnetic field components are used for the ray-tracing calculation at present. The volume-averaged beta for the shots applied for modeling in this work is at most 1%, which indicates that the magnetic field outside the LCFS is approximated to the vacuum magnetic field. Furthermore, in a case when the neutral beam injection heating is applied, the beam component can modify the pressure profile and the best fit pressure profile can be inconsistent with that expected from kinetic thermal beta. The difference of refraction of rays in the cases with and without accounting periphery plasma outside the LCFS should be expected especially in higher density plasmas, although the effect cannot be spatially noticeable under the plasma parameters discussed in this paper due to the current resolution of the ECE diagnostics.

Injection settings for ECH are determined from ECH setting logs produced each shot. The logs include input power, injection timing, target positions, polarization states, angles of final steering antennas, and Gaussian beam parameters for each EC beam line.

Secondly, the mode purity is calculated with the 1D full-wave equation along the propagating direction with the cold plasma dielectric tensor, which is summarized in Appendix B. Because contents of each mode excited at the plasma core depend not only on the injection angle and the polarization states but also on the density gradient and the magnetic shear in the interface region [23, 24], electromagnetic waves with all three components are solved along the propagating direction from the antenna to the target point. In this calculation, the extrapolated equilibrium map is used and all three components of the magnetic field are taken into account to include the density gradient and the magnetic shear. The electric field components perpendicular to the propagating direction are decomposed into two orthogonal components with real and imaginary parts, respectively, in order to express the polarization state of the electric field. The local dispersion relation using the local n_e and the local magnetic field gives the relation between the O-mode and the X-mode electric fields. Each local mode content is determined by checking orthogonality between the polarization state of the local electric field and that of the O- or X-mode electric field, respectively [25], i.e., the local electric field can be decomposed into the orthogonal O- and X-mode electric fields. Each mode content converges to a certain value as the EC wave propagates through the plasma interface region. The excited modes with the fixed O/X mode ratio propagate to the plasma core region, where the wave numbers for both modes are well separated to satisfy $|k_O - k_X|\lambda_s \gg 1$, where k_O and k_X are the wave numbers for the O mode and the X mode, respectively, and λ_s is the scale length of the magnetic shear.

Thirdly, ray-tracing calculations are executed to obtain the power deposition profiles on each magnetic flux surface labeled by r_{eff}. The injection Gaussian beam is modeled as multiple rays equally distributed with the Gaussian-weighted power fraction for each beam segment. The propagation of each ray is based on the model of geometrical optics with the

cold plasma dispersion relation to save the computer resources. The absorption of each ray is calculated according to the quasi-perpendicular weakly relativistic model [26]. The neglected Doppler shift may affect absorption in the case of oblique propagation of the beams. A possible maximum shift of the absorption location with respect to the magnetic flux surfaces is estimated to be $\Delta(r_{\mathrm{eff}}/a_{99}) \sim 0.1$ for high temperature plasmas. Interactions between the rays in their propagation and absorption processes are not included as are done in the beam-tracing or the quasi-optical beam-tracing code [27, 28, 29]. For the ray-tracing calculations, local physical quantities, such as $T_{\mathrm{e}}(r_{\mathrm{eff}})$ and $n_{\mathrm{e}}(r_{\mathrm{eff}})$, are obtained by interpolating r_{eff} from the mesh data of the 3D equilibrium mapping, assuming that the T_{e} and n_{e} are constant over a flux surface. The vacuum magnetic field components are also interpolated from the mesh data registered. The absolute values of the power deposition profiles for the O mode and the X mode are obtained by the power ratios between those modes calculated with the 1D full-wave equation described above.

Finally, the ray-tracing calculation results, which are composed of the injection settings, the mode purity, the ray trajectories, the extended equilibrium mapping, and the power deposition profiles, are processed as the unified format for the LHD database and registered in the LHD database.

These calculations are automatically executed for each shot and each time slice of the Thomson scattering diagnostic measurement during a pulse, and they are computed in parallel with multiple CPU cores in the *AutoAna* system. This fast calculation scheme together with comparisons with the Thomson scattering diagnostic measurement or the electron cyclotron emission (ECE) diagnostic enables the seeking of the optimal injection settings for a required power deposition profile on a shot-by-shot basis during ECH experiments in the LHD.

LHDGauss will be introduced into the *TASK3D-a* [20], the integrated transport analysis suite, as an ECH module so that the calculated power deposition profile is used for the heat transport study for LHD plasmas.

3. ECH experiments with LHDGauss

In this section, ECE diagnostics signals [30, 31] along with the Thomson scattering diagnostics, and absorbed power estimated with the diamagnetic flux measurements [31, 32] are compared with the results of *LHDGauss* for its validation. Dependence of absorbed power on mode purity is also discussed.

3.1. Comparison with ECE and Thomson scattering diagnostics

Figures 2(a)-(e) show (a) phases and (b) amplitudes of ECE FFT signals at a MECH frequency of 25 Hz, (c) T_{e} measured with the Thomson scattering diagnostics, and (d) power deposition and (e) absorbed power calculated by *LHDGauss* as a function of r_{eff}/a_{99} for five different target (focal) positions labeled as $Z_{\mathrm{f}} = -0.02, -0.07, -0.12, -0.17,$ and -0.22 m, where Z_{f} denotes the Z (vertical) coordinate of the target position. The target position $(R_{\mathrm{f}}, T_{\mathrm{f}}, Z_{\mathrm{f}})$ is defined on the plane perpendicular to the radial (R) direction from the center axis to the outer
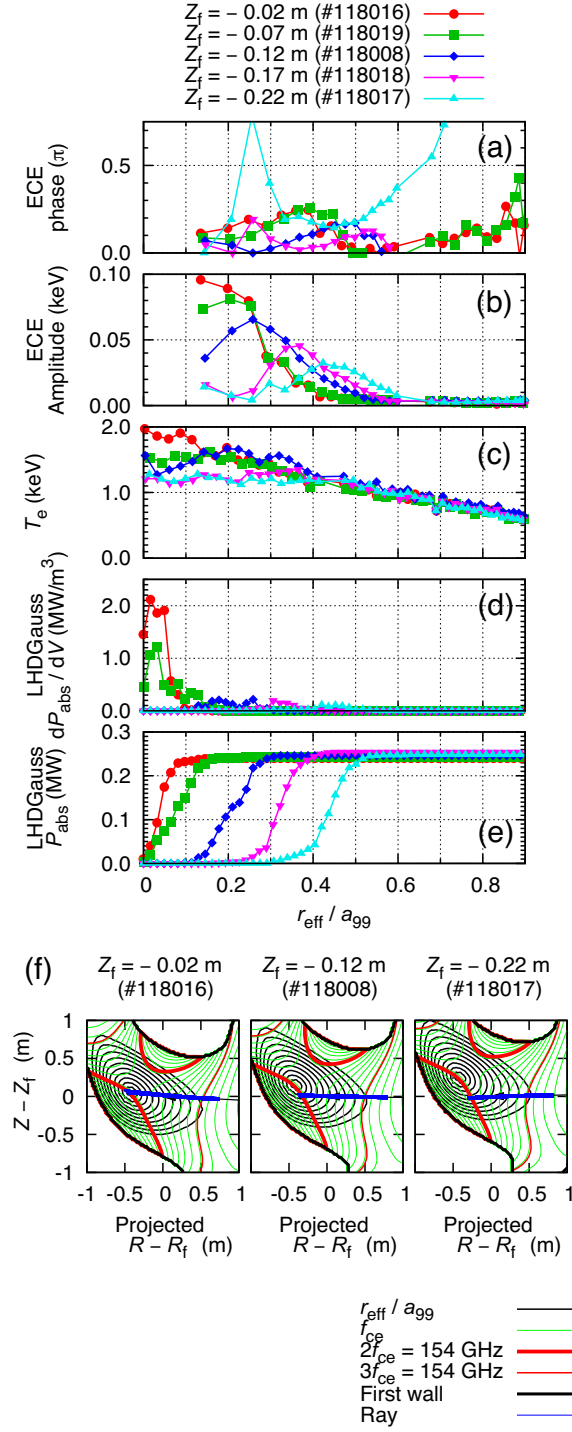
Figure 2. (a) Phases and (b) amplitudes of ECE signals at the ECH modulation frequency of 25 Hz, (c) T_e measured with the Thomson scattering diagnostics, and (d) power deposition and (e) absorbed power calculated by *LHDGauss* as a function of r_{eff}/a_{99} for five different focal positions in Z (vertical) direction. The ECH power from one 154 GHz beam line was modulated at 25 Hz. (f) Projected ray trajectories for the three different focal positions are also shown along with magnetic flux surfaces and EC resonance lines.

port #2 center and the origin of the plane is set at $(R_f, T_f, Z_f) = (3.9, 0, 0)$ m. Here, a_{99} denotes the effective minor radius which encloses 99% of the total electron pressure. Z_f was scanned by adjusting the injection antenna while the radial R_f and the toroidal T_f components of the target position were fixed at $(R_f, T_f) = (3.9, 0.42)$ m. The ECH power from one 154 GHz beam line is modulated at 25 Hz to obtain the modulated ECE signals and is horizontally launched from the outer port #2. Figure 2(f) shows projected ray trajectories for the three different target positions on the plane consisting of two orthogonal basis vectors, $e_z \times (e_z \times e_{inj})$ and e_z, where e_z denotes the unit vector in the vertical (Z) direction and e_{inj} denotes the unit vector in the direction from the injection antenna center to the target position. Contours of magnetic flux surfaces r_{eff}/a_{99} and the electron cyclotron frequencies f_{ce}, the second and third harmonic electron cyclotron resonance frequency lines ($2f_{ce} = 154$ GHz and $3f_{ce} = 154$ GHz), and the first wall are also superimposed on the planes. Figure 2(f) indicates that the rays with the X mode are not refracted significantly due to the relatively low line-averaged electron density $n_{e,fir} = 2.5 \times 10^{19}$ m^{-3} for the 154 GHz EC wave. The power deposition profiles of the second harmonic X mode show peaked profiles at around Z_f, which are mapped into each r_{eff}, respectively, as shown in figure 2(d), while the absorbed power of approximately 0.25 MW is less than the injection power of 0.4 MW, as shown in figure 2(e), due to the unoptimized injection polarization, which does not result in excitation of pure X mode at the resonance layer. It is found that the positions of the deposition peaks in *LHDGauss* agree well with those of the phase bottoms and the amplitude peaks in the ECE diagnostics in the cases of $Z_f = -0.12, -0.17,$ and -0.22 m, as shown in figures 2(a), (b), and (d). Since the ECE diagnostics are not available near the magnetic axis, the ECE data only indicate that the power absorption is inside $r_{eff}/a_{99} \sim 0.2$ for the cases of $Z_f = -0.02$ and -0.07 m, respectively, but the most center-peaked T_e profile is confirmed in the case of $Z_f = -0.02$ m, as shown in figure 2(c), which coincides with the ray-tracing calculation results of on-axis heating. It is observed that the radial widths of the ECE amplitudes are wider than the widths of the absorption profiles by *LHDGauss*. The widths of the ECE signals are affected significantly by the perpendicular heat transport especially in such low modulation frequency [33]. The effect will be analyzed in the future by using the transport code *TASK3D-a*, in which *LHDGauss* will be incorporated as the input for a heat source.

3.2. Comparison with diamagnetic flux measurement

Figure 3 shows the absorbed power estimated with the diamagnetic flux measurement and the absorbed power calculated by *LHDGauss* for each beam line as a function of line-averaged electron density $n_{e,fir}$ measured by the FIR laser interferometer. In these experiments all the injection antennas were targeted toward the vacuum magnetic axis. The absorbed power is experimentally estimated by calculating change in time derivative of the plasma stored energy just before and after MECH on/off timing. The 2-O port 77 GHz injection system, horizontally launched from the outer port #2, has high absorption rates in relatively high $n_{e,fir}$ region ($< 1.5 \times 10^{19}$ m^{-3}) although the rays are refracted and deviated from the magnetic axis for high n_e plasmas. The beams from the 2-O port 154 GHz injection systems keep full
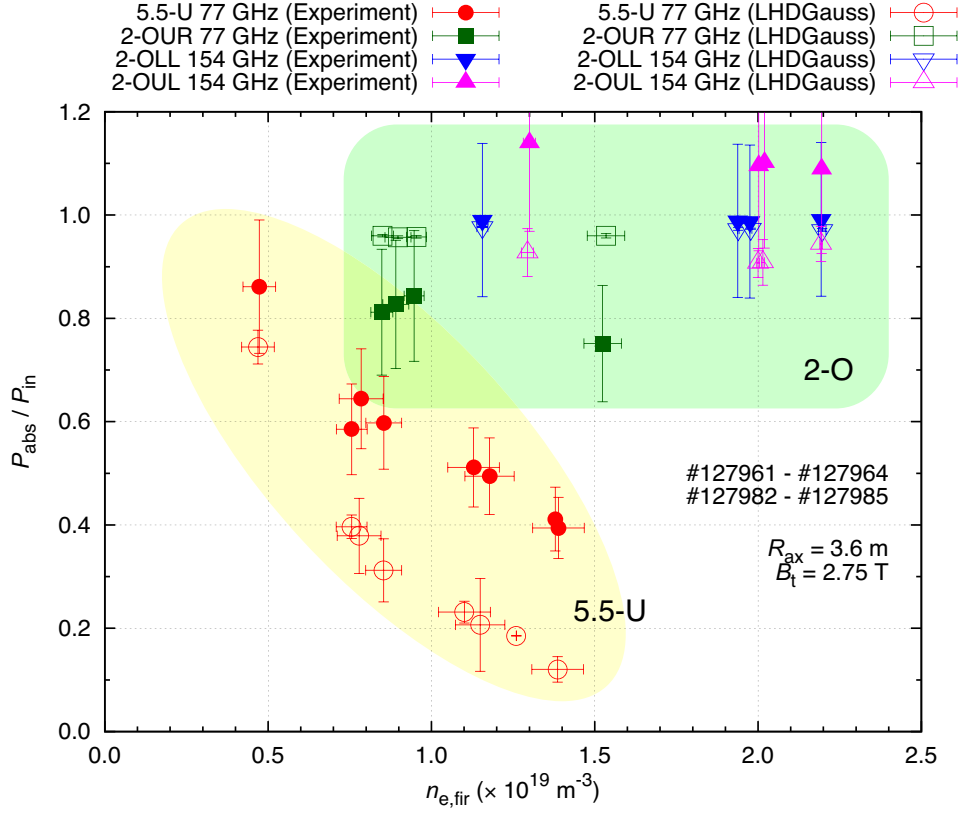
Figure 3. Absorbed power estimated with the diamagnetic flux measurement and that calculated by *LHDGauss* from a single pass for each beam line as a function of $n_{e,fir}$. In these experiments, all the injection antennas were aligned for the vacuum magnetic configuration and the focal positions were set at the vacuum magnetic axis.

absorption rates since the rays are not refracted for the range of $n_{e,fir}$, as shown in figure 3. The one 154 GHz EC beam line (2-OUL) shows the absorption rates above 100%, but those can be attributed to the errors arising from the uncertainty in the estimation of both the absorbed power P_{abs} and the input power P_{in}. Here, "2-OUL" denotes that the end of the waveguide locates at the upper left side of the outer port #2 seen from the outside of the LHD vacuum vessel. It is found that the rays from the 5.5-U port 77 GHz injection system, launched almost vertically from the upper port #5.5, are refracted in high n_e plasmas, which causes degradation of the power absorption.

The ray-tracing calculations with *LHDGauss* show that the absorption rates are almost 100% for the 2-O EC beam lines, which is in rough agreement with the experimental values of the high absorption rates. However, the deviations are large between *LHDGauss* and the experiment for the 5.5-U EC beam line. One of the reasons is that the effect of multiple reflection of rays is not included in *LHDGauss* although single-pass absorption is weak for the 5.5-U beam line in this experiment. The injection antenna was aligned for on-axis heating in the vacuum magnetic field configuration, which resulted in refraction of the rays and their deviation from the EC resonance layer. The effect of the multiple reflection can be recognized clearly in figure 4, which shows modulated components of ECE amplitudes for the 5.5-U and
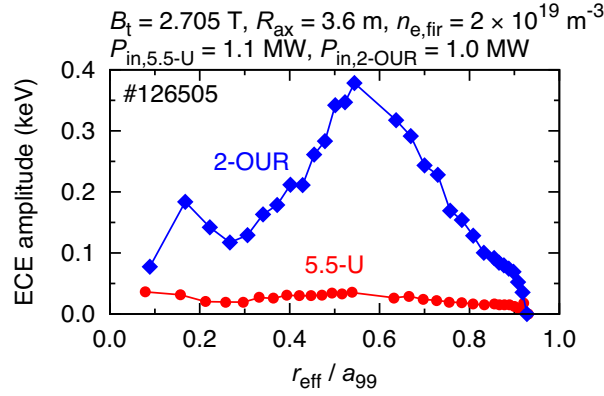
Figure 4. Modulated components of ECE amplitudes for the 5.5-U and the 2-OUR EC beam lines, respectively, as a function of r_{eff}/a_{99}.

the 2-OUR ECH, respectively, as a function of r_{eff}/a_{99}. In this discharge, the absorbed power from the 5.5-U ECH is estimated to be almost half of that from the 2-OUR ECH although the two EC beam lines each have almost the same injection power of as large as 1 MW. Again, the injection antennas were aligned for the vacuum magnetic axis. As shown in figure 4, the peaked profile at $r_{\mathrm{eff}}/a_{99} \sim 0.55$ is clearly observed for the 2-OUR ECH, while the almost flat profile is observed for the 5.5-U ECH. This fact suggests that the main part of the injected EC beam from the 5.5-U port does not reach the resonance layer with the single pass, while the injected EC beam from the 2-O port does. This gives rise to a high demand for fine tuning of the 5.5-U ECH injection in order to compensate the refraction effect so as to keep on-axis heating under high n_e plasmas. Eventually, since the effect of the multiple reflection is difficult to take into account for ray-tracing calculations due to complicated inner structures of the LHD, the absorption rates tend to be underestimated from the measurement unless single-pass absorption for all rays is achieved.

3.3. Dependence of absorbed power on mode purity

Dependence of absorbed power on mode purity was evaluated with *LHDGauss* that includes the mode purity calculation. Figure 5 shows the calculation results of the 1D full-wave equations along the propagating direction from the injection antenna to the absorption target point for two different polarization states, (1) $(\alpha, \beta) = (46.21°, 4.88°)$ and (2) $(\alpha, \beta) = (25.06°, -0.3°)$, which are set, respectively, by the polarizers installed at the miter bends in the 5.5-U ECH transmission line. Plotted are (a) n_e and r_{eff}/a_{99}, (b) the magnetic field strength $|B|$, the magnetic shear angle ϕ and the propagation angle to the magnetic field θ, (c) amplitudes of the electric field components $|E_{x'}|$ and $|E_{y'}|$ and those of the O-mode electric field components $|E_{\mathrm{O},x'}|$ and $|E_{\mathrm{O},y'}|$, (d) the polarization state of the electric field (α, β) and that of the O-mode electric field $(\alpha_{\mathrm{O}}, \beta_{\mathrm{O}})$, and (e) the mode purity. In these cases, the calculations are terminated before the right-handed wave cutoff point. $r_{\mathrm{eff}}/a_{99} > 1$ (the outside of the LCFS) shows the extrapolated virtual magnetic flux surfaces. In these calculations, the Cartesian coordinate
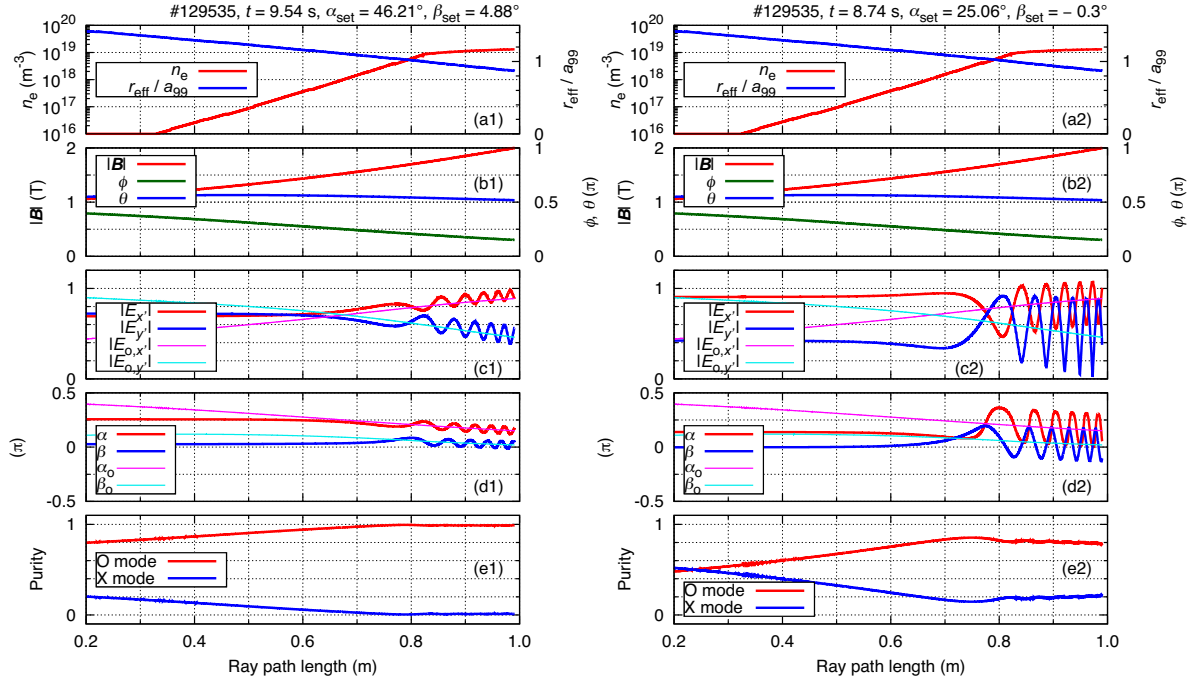
Figure 5. Calculation results of 1D full-wave equations along the propagating direction from the injection antenna to the absorption target point for two different polarization states, (1) $(\alpha, \beta) = (46.21°, 4.88°)$ and (2) $(\alpha, \beta) = (25.06°, -0.3°)$, set by the polarizers installed at the miter bends in the 5.5-U 77 GHz ECH transmission line. (a) n_e and r_{eff}/a_{99}, (b) the magnetic field strength $|B|$, the magnetic shear angle ϕ, and the propagation angle to the magnetic field θ, (c) amplitudes of the electric field components $|E_{x'}|$ and $|E_{y'}|$ and those of the O-mode electric field components $|E_{O,x'}|$ and $|E_{O,y'}|$, (d) the polarization state of the electric fields (α, β) and that of the O-mode electric fields (α_O, β_O), and (e) the mode purity. In these cases, the calculations are terminated before the right-handed wave cutoff point. $r_{eff}/a_{99} > 1$ (the outside of the LCFS) shows the extrapolated virtual magnetic flux surfaces.

system is defined by the following unit vectors:

$$e_{x'} = \frac{-k \times (k \times \varphi)}{|k \times (k \times \varphi)|}, \qquad e_{y'} = \frac{k \times \varphi}{|k \times \varphi|}, \qquad e_{z'} = \frac{k}{|k|},$$

where k and φ denote unit vectors of the wave number and the toroidal direction, respectively. This coordinate system is independent on the static magnetic field in order to define the polarization of the injected millimeter waves on the plane perpendicular to k. According to this coordinate system, ϕ and θ are represented by

$$\phi = \tan^{-1} \frac{B_{y'}}{B_{x'}}, \qquad \theta = \cos^{-1} \frac{B_{z'}}{\sqrt{B_{x'}^2 + B_{y'}^2 + B_{z'}^2}}.$$

α denotes the rotation angle of the major axis of the polarization ellipse and β denotes the ellipticity. Then, the polarization parameters (α, β) of the electric field perpendicular to the k are obtained by

$$\tan 2\alpha = \tan 2\gamma \cos \delta, \qquad \sin 2\beta = \sin 2\gamma \sin \delta,$$

where $\gamma = \tan^{-1}(|E_{y'}|/|E_{x'}|)$ and $\delta = \arg E_{y'} - \arg E_{x'}$. Due to orthogonality of polarization, the O/X-mode purity is obtained by

$$\eta_\sigma = \cos^2(\alpha - \alpha_\sigma)\cos^2(\beta - \beta_\sigma) + \sin^2(\alpha - \alpha_\sigma)\sin^2(\beta + \beta_\sigma),$$

where σ denotes the mode "O" or "X" and the polarization state $(\alpha_\sigma, \beta_\sigma)$ of the electric field E_σ is derived from the local dispersion relation. $\eta_\sigma = 1$ if the two states (α, β) and $(\alpha_\sigma, \beta_\sigma)$ are identical and $\eta_\sigma = 0$ if they are orthogonal [25].

As shown in figures 5(a1)-(e1), the injected millimeter wave with the given polarization couples to electromagnetic waves with the initial polarization remaining in the extremely low density region of $n_e < 10^{18}$ m^{-3}. The electromagnetic wave has no inherent mode such as the O mode and the X mode, where the two modes are degenerate due to the low density plasma. It is found that the electromagnetic wave gradually couples to the O mode and propagates into the plasma peripheral region. The O mode purity reaches almost unity and it remains inside the LCFS. In the case of nearly perpendicular injection ($\theta \sim 90°$) from the 5.5-U port, it is expected that the linearly polarized wave ($\beta \sim 0°$) with α same as ϕ can excite pure O mode at the peripheral region, where $\phi \sim 45°$. That is why the almost 100% O mode content is obtained by the linearly polarized wave with optimum $\alpha_{set} \sim 45°$. However, as shown in figures 5(a2)-(e2), the O mode content is obtained at less than unity due to the inappropriate polarization state of $\alpha_{set} \sim 25°$. Oscillating electric fields in the propagating direction are observed inside the plasma region due to different wave numbers for each mode.

These calculations may be more useful in a situation in which a magnetic shear and a density gradient are larger. Due to the interface region, the exact plasma boundary no longer exists, where the injected millimeter wave couples to the plasma wave. The optimal injection polarization cannot be determined with the magnetic shear angle at the plasma boundary. The optimal injection polarization can be finely searched by using this calculation method, which may suggest that elliptical polarization is needed even for a perpendicular injection case.

Figure 6 shows (a) the absorption rate and (b) the mode purity for the 5.5-U ECH as a function of α with β fixed at $\beta \simeq 0°$. The absorption rates are experimentally estimated at the ECH turn-on and -off timing, which is compared with the ray-tracing calculation results with *LHDGauss*. The absorption rates calculated with *LHDGauss* agree well with the experimental data due to inclusion of the mode content analyses. The evaluated absorption rates are represented by a sinusoidal dependence with a suitable maximum value fitted. Small deviations between the mode purity data and the sinusoidal function are considered to be a result of the effect of finite ellipticity necessary for oblique propagation as in the injection from the 5.5-U port.

4. Optimization of ECH injection settings

Extension of the high temperature regime for the LHD was successfully achieved by utilization of *LHDGauss* upgraded with the rapid post-processing magnetic coordinate mapping system. The injection antennas were firstly aligned for the vacuum magnetic axis. Then, the injection antennas were aligned for the high temperature plasma, which was based
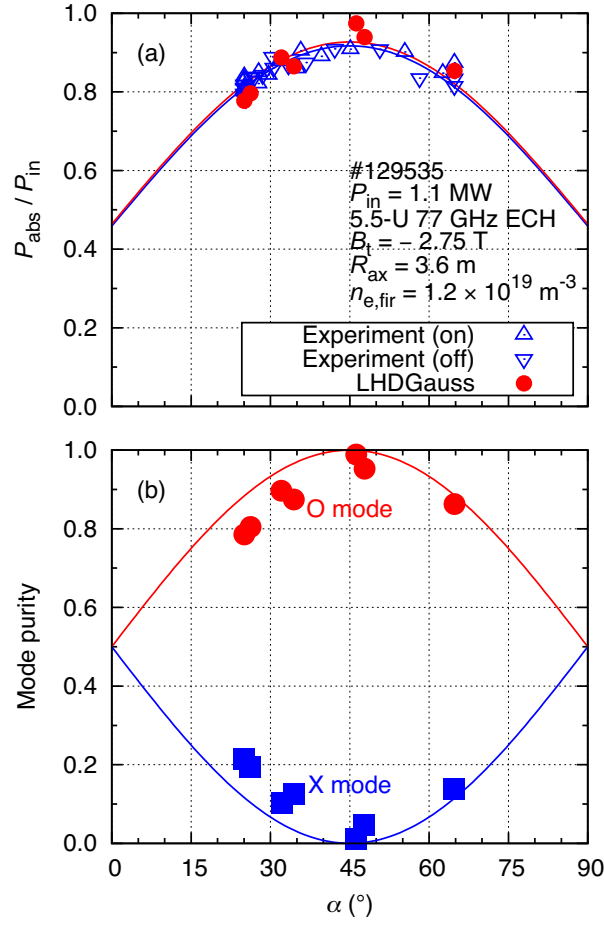
Figure 6. (a) Absorption rate and (b) mode purity as a function of polarization angle α. Absorption rates are estimated at ECH turn-on and -off timing, which are compared with the ray-tracing calculation results using *LHDGauss* with the mode purity analyses included. The curves plotted in (a) are functions of $\eta_{max} \sin^2(\alpha + \pi/4)$ with η_{max} fitted with the experimental data or the calculation data, respectively. The O-mode purity is represented as $\sin^2(\alpha + \pi/4)$, while the X-mode purity is represented as $1 - \sin^2(\alpha + \pi/4)$.

on the ray-tracing calculations of the previous discharges of the high temperature plasmas with the same condition except for the injection antennas.

Figures 7 and 8 show ray-tracing calculation results (1) before and (2) after tuning the injection antennas of the 5.5-U and the 2-OUR EC beam lines, respectively, for the high temperature plasma under the experimental n_e and T_e profiles along with the 3D equilibrium mapping. In figure 7, rays are projected on two planes: (a) the plane consisting of two orthogonal basis vectors, e_r and $(e_{inj} \times e_r) \times e_r$, and (b) the plane consisting of two orthogonal basis vectors, e_{tor} and $(e_{inj} \times e_{tor}) \times e_{tor}$, where e_r denotes the unit vector in the radial direction at the 5.5-U port center, e_{tor} denotes the unit vector in the toroidal direction at the 5.5-U port center, and e_{inj} denotes the unit vector in the direction from the injection antenna center to the target point. The contours of magnetic flux surfaces r_{eff}/a_{99} and the electron cyclotron frequencies f_{ce}, lines of the right-handed wave cutoff frequency f_{rc}, the upper hybrid resonance frequency f_{uh}, and the electron cyclotron resonance frequency coincide with 77 GHz, and
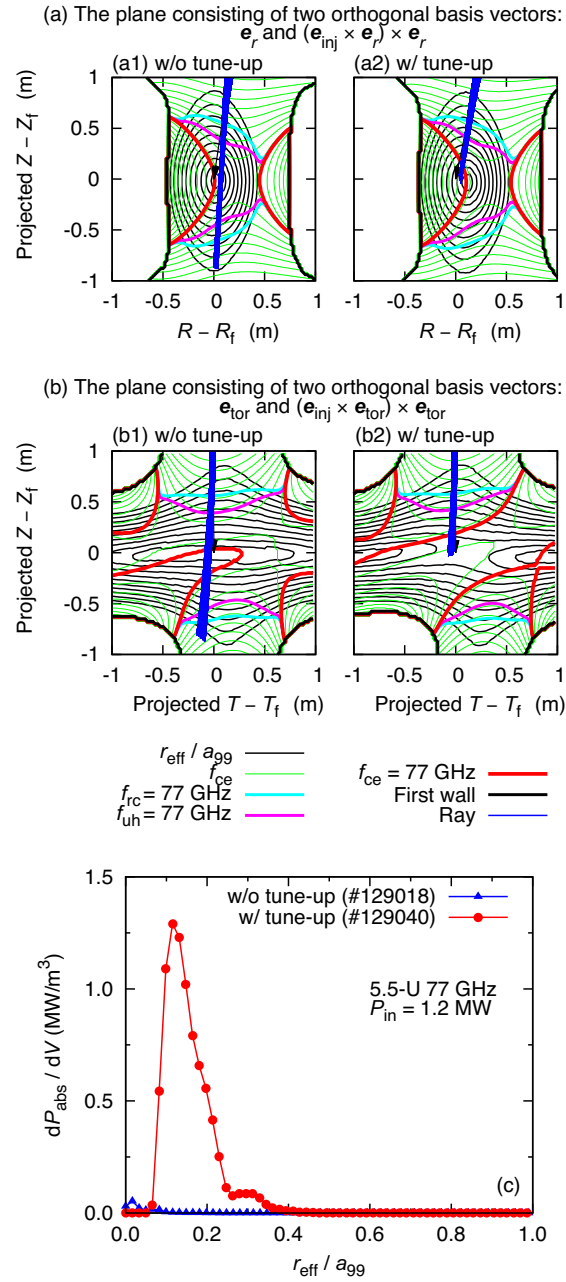
Figure 7. Ray-tracing calculation results (1) before and (2) after tuning the injection antenna of the 5.5-U 77 GHz EC beam line for the high temperature plasma under the experimental n_e and T_e profiles along with the 3D equilibrium mapping. Rays are projected on two planes: (a) the plane consisting of two orthogonal basis vectors, e_r and $(e_{inj} \times e_r) \times e_r$, and (b) the plane consisting of two orthogonal basis vectors, e_{tor} and $(e_{inj} \times e_{tor}) \times e_{tor}$, where e_r denotes the unit vector in the radial direction at the 5.5-U port center, e_{tor} denotes the unit vector in the toroidal direction at the 5.5-U port center, and e_{inj} denotes the unit vector in the direction from the injection antenna center to the target point. Arrowheads denote target points. Contours of r_{eff}/a_{99} and f_{ce}, lines of f_{rc}, f_{uh}, and f_{ce} for 77 GHz, and the first wall are also superimposed on the planes. The resultant power deposition profiles as a function of r_{eff}/a_{99} are shown in (c).

the first wall are also superimposed on the planes. The resultant power deposition profiles as a function of $r_{\rm eff}/a_{99}$ are shown in (c), which indicates that tuning the injection antenna contributes to high power deposition near the magnetic axis, compared to no deposition in the case without the tuning. In figure 8, rays are projected on two planes: (a) the plane consisting of two orthogonal basis vectors, $e_z \times (e_z \times e_{\rm inj})$ and e_z, and (b) the plane consisting of two orthogonal basis vectors, $e_{\rm tor} \times (e_{\rm tor} \times e_{\rm inj})$ and $e_{\rm tor}$, where e_z denotes the unit vector in the vertical direction, $e_{\rm tor}$ denotes the unit vector in the toroidal direction at the 2-O port center, and $e_{\rm inj}$ denotes the unit vector in the direction from the injection antenna center to the target point. The contours of $r_{\rm eff}/a_{99}$ and $f_{\rm ce}$ and the lines of resonance and cutoff for 77 GHz are also plotted as in figure 7. The resultant power deposition profiles as a function of $r_{\rm eff}/a_{99}$ are shown in (c), which indicates that tuning the injection antenna contributes to on-axis heating.

Figure 9 shows $T_{\rm e}$ and $n_{\rm e}$ profiles as a function of $r_{\rm eff}/a_{99}$ in the cases with and without tuning the injection antennas for all the EC beam lines. Almost maximum power as large as 5.1 MW with all the EC beam lines is injected to the high $T_{\rm i}$ plasma with $T_{\rm i0} = 5$ keV for the case without tuning so far. Besides, clear increase in $T_{\rm e0}$ up to 7.5 keV is observed due to tuning the injection antennas based on the ray-tracing calculations with *LHDGauss*. This outstanding result is an extension from the conventional high $T_{\rm i}$ plasmas in the LHD [34].

5. Summary

The ray-tracing code *LHDGauss* has been upgraded to include the rapid post-processing 3D equilibrium mapping system. By using the interpolated and extrapolated 3D equilibrium mapping data, the mode contents are determined through solving the 1D full-wave equation along the injection propagating direction from the antenna to the absorption target point. The $n_{\rm e}$ profiles and the magnetic shear affect polarization of the injected electric fields and determine optimal coupling to plasma waves, thereby changing the absorbed power, which is confirmed in experiments. The optimal coupling can be solved by using this calculation process and this consideration may be more crucial if a magnetic shear and a density gradient are larger, where elliptical polarization is needed even for a perpendicular beam line.

The ray-tracing calculation results are extensively compared with the LHD experiments. Deposition peak positions calculated with *LHDGauss* show good agreement with the phase bottoms and the amplitude peaks in the ECE diagnostics in the case of off-axis heating. On-axis heating cases confirmed with the Thomson scattering diagnostics coincide with the ray-tracing calculation results. The measured absorbed power is comparable to the ray-tracing calculation results if the single-pass absorption rate is almost 100%. The calculated absorption rate tends to be underestimated from the measurement if the single-pass absorption is weak due to lack of the multi-pass absorption effect, which is not implemented in *LHDGauss*.

Power deposition profiles calculated at each shot and each time slice of the Thomson scattering diagnostics are automatically registered in the LHD database, which contributed to searching optimal ECH injection settings during experiments. Adjustment of the injection settings with *LHDGauss* resulted in successful increase of $T_{\rm e0}$ up to 7.5 keV for the high $T_{\rm i}$ plasma, which is an extension of the LHD operational regime. In the near future, higher $T_{\rm e}$

can be expected by optimizing not only an injection antenna but also injection polarization for each EC wave with the help of *LHDGauss*.

Acknowledgments

Appendix A. Interpolation and extrapolation of the 3D equilibrium mapping data

Interpolation and extrapolation of the 3D equilibrium mapping data *TSMESH* that relates $(x(r, \varphi), y(r, \varphi), z)$ to r_{eff} are conducted by fitting a 3D bi-quadratic formula whose coefficients are deduced from minimizing the fitting error using the singular value decomposition (SVD) method. Let us suppose that r_{eff} exists in the outside of the LCFS and the extrapolation is executable to the outside of the LCFS although the extrapolation does not have any physical meanings at all. r_{eff} can be expressed in the bi-quadratic formula such that

$$r_{\text{eff}} = \sum_{j=1}^{10} a_j \xi_j, \tag{A.1}$$

where $a_1 = 1$, $a_2 = x$, $a_3 = y$, $a_4 = z$, $a_5 = x^2$, $a_6 = y^2$, $a_7 = z^2$, $a_8 = xy$, $a_9 = yz$, and $a_{10} = zx$, and ξ_j denotes their coefficients, respectively. In a set of sampled mesh points near the object point in the 3D equilibrium mapping space, i.e., $(a_{ij}, r_{\text{eff},i})$ $(i = 1, 2, \cdots, m)$, where m denotes the number of the sampled data points for j and is chosen to be $m = 512 (\gg 10)$, equation A.1 is rewritten as

$$r_{\text{eff},i} = \sum_{j=1}^{10} a_{ij} \xi_j,$$

or in a matrix form

$$\boldsymbol{\zeta} = A\boldsymbol{\xi},$$

where $\boldsymbol{\zeta} = (r_{\text{eff},1}, r_{\text{eff},2}, \cdots, r_{\text{eff},m})^\top$, $\boldsymbol{\xi} = (\xi_1, \xi_2, \cdots, \xi_{10})^\top$, and $A = (a_{ij})_{1 \le i \le m, 1 \le j \le 10}$. Then, the coefficients column vector $\boldsymbol{\xi}$ is obtained with the Moore-Penrose pseudo-inverse matrix of A from

$$\boldsymbol{\xi} = A^+ \boldsymbol{\zeta}.$$

The pseudo-inverse matrix provides a solution to the least squares problem, where the $\boldsymbol{\xi}$ is solved by minimizing

$$\|A\boldsymbol{\xi} - \boldsymbol{\zeta}\|^2 = (A\boldsymbol{\xi} - \boldsymbol{\zeta})^\top (A\boldsymbol{\xi} - \boldsymbol{\zeta}).$$

SVD provides an accurate way to compute the pseudo-inverse matrix along with an optimal solution to the least squares problem. SVD is implemented numerically in most computer languages as a function or a module. Interpolation and extrapolation for a given point can

be executed in this way. Figure A1 illustrates original and extrapolated virtual magnetic flux surfaces r_{eff}/a_{99} on poloidal planes, for example, at (a) $\varphi = 0°$, (b) $\varphi = 9°$, and (c) $\varphi = 18°$. The r_{eff}/a_{99} contours near and outside the LCFS are smoothly generated, although those near the first wall away from the LCFS are not smooth lines.

Appendix B. Polarization in a non-uniform sheared magnetic field and a non-uniform density plasma

When the magnetic field and the electron density are non-uniform and are presumed to be a weak function of the propagating direction z', the magnetic field is given by

$$
\boldsymbol{B}(z') = B_0(z')\boldsymbol{b}(z') = B_0(z') \begin{pmatrix} b_{x'}(z') \\ b_{y'}(z') \\ b_{z'}(z') \end{pmatrix},
$$

where B_0 and $\boldsymbol{b}$ are the strength and the unit vector of $\boldsymbol{B}$, respectively. From the Maxwell equations and equations of motion,

$$
\nabla \times \nabla \times \tilde{\boldsymbol{E}} = \frac{\omega^2}{c^2} \left[\mathsf{I} - \frac{\omega_{\text{pe}}^2}{\omega^2} \left(\mathsf{I} + \mathrm{i}\frac{\Omega_{\text{e}}}{\omega}\boldsymbol{b}\times \right)^{-1} \right] \cdot \tilde{\boldsymbol{E}}
$$

is obtained. Here, I, ω_{pe}, and Ω_{e} are a unit tensor, the plasma frequency for electrons, and the cyclotron frequency for electrons. The 1D full wave equation along with the wave propagation direction (z') is written as

$$
\begin{aligned}
&\delta_{iz'}\frac{\partial^2 \tilde{E}_{z'}}{\partial z'^2} - \frac{\partial^2 \tilde{E}_i}{\partial z'^2} \\
&= \frac{\omega^2}{c^2} \left[\delta_{ij} - \frac{\omega_{\text{pe}}^2}{\omega^2 - \Omega_{\text{e}}^2} \left\{ \delta_{ij} - \left(\frac{\Omega_{\text{e}}}{\omega}\right)^2 b_i b_j + \mathrm{i}\left(\frac{\Omega_{\text{e}}}{\omega}\right)\varepsilon_{ijk}b_k \right\} \right] \tilde{E}_j \\
&= \frac{\omega^2}{c^2}\epsilon_{ij}\tilde{E}_j,
\end{aligned}
$$

where δ_{ij}, ε_{ijk}, and ϵ_{ij} are the Kronecker's delta, the Levi-Civita symbol, and the cold plasma dielectric tensor, respectively. The electric field is excited at the final mirror location of the injection antenna according to the injection polarization. Evolution of the electric field can be obtained by solving this equation.

The local dispersion relation can be obtained from the above equation by assuming the uniform fields and density and also by deleting $\tilde{E}_{z'}$. The relation between $\tilde{E}_{x'}$ and $\tilde{E}_{y'}$ is given by

$$
\begin{pmatrix} \epsilon_{x'x'} - \epsilon_{x'z'}\epsilon_{z'x'}/\epsilon_{z'z'} - n^2 & \epsilon_{x'y'} - \epsilon_{x'z'}\epsilon_{z'y'}/\epsilon_{z'z'} \\ \epsilon_{y'x'} - \epsilon_{y'z'}\epsilon_{z'x'}/\epsilon_{z'z'} & \epsilon_{y'y'} - \epsilon_{y'z'}\epsilon_{z'y'}/\epsilon_{z'z'} - n^2 \end{pmatrix} \begin{pmatrix} \tilde{E}_{x'} \\ \tilde{E}_{y'} \end{pmatrix} = 0.
$$

Having a non-trivial solution requires that the determinant of coefficients vanishes, which gives the cold plasma dispersion relation with eigenvalues n_σ^2, where σ denotes the mode "O" or "X." Then the polarization of each mode is obtained from

$$
\begin{pmatrix} \tilde{E}_{\sigma,x'} \\ \tilde{E}_{\sigma,y'} \end{pmatrix} \propto \begin{pmatrix} \epsilon_{x'z'}\epsilon_{z'y'} - \epsilon_{z'z'}\epsilon_{x'y'} \\ \epsilon_{z'z'}(\epsilon_{x'x'} - n_\sigma^2) - \epsilon_{x'z'}\epsilon_{z'x'} \end{pmatrix}.
$$

References

[1] Yoshimura Y. *et al* 2010 *Fusion Sci. Technol.* **58** 551

[2] Yoshimura Y. *et al* 2005 *J. Phys.: Conf. Ser.* **25** 189

[3] Komori A. and Morisaki T. 2014 *J. Phys.: Conf. Ser.* **565** 012017

[4] Petty C. C. and Luce T. C. 1994 *Nucl. Fusion* **34** 121

[5] Ida K. *et al* 2013 *New J. Phys.* **15** 013061

[6] Inagaki S. *et al* 2013 *Nucl. Fusion* **53** 113006

[7] Suzuki C., Ida K., Suzuki Y., Yoshida M., Emoto M., and Yokoyama M. 2013 *Plasma Phys. Control. Fusion* **55** 014016

[8] Hirshman S. P. and Whitson J. C. 1983 *Phys. Fluids* **26** 3553

[9] Yamada I. *et al* 2012 *JINST* **7** C05007

[10] Emoto M., Ida K., Suzuki C., Yoshida M., Akiyama T., Nakamura Y., Sakamoto R., Yokoyama M., and Yoshinuma M. 2014 *Fusion Eng. Des.* **89** 758

[11] Kubo S. *et al* 2003 *Proc. 11th Int. Congress on Plasma Physics, AIP Conf. Proc.* **669** 187.

[12] Kubo S. *et al* 2005 *Plasma Phys. Control. Fusion* **47** A81

[13] Igami H. *et al* 2012 *Plasma Fusion Res.* **7** 2402110

[14] Prater R. *et al* 2008 *Nucl. Fusion* **48** 035006

[15] Marushchenko N. B., Erckmann V., Hartfuss H. J., Hirsch M., Laqua H. P., Maassberg H., and Turkin Y. 2007 *Plasma Fus. Res.* **2** S1129

[16] Marushchenko N. B., Turkin Y., and Maassberg H. 2014 *Comput. Phys. Commun.* **185** 165

[17] Takahashi H. *et al* 2014 *Phys. Plasmas* **21** 061506

[18] Shimozuma T. *et al* 2010 *Fusion Sci. Technol.* **58** 530

[19] Shimozuma T. *et al* 2009 *J. Microwave Power Electromag. Energy* **43** 60

[20] Yokoyama M. *et al* 2013 *Plasma Fusion Res.* **8** 2403016

[21] Ida K. *et al* 2003 *Phys. Rev. Lett.* **91** 085003

[22] Shimozuma T. *et al* 2008 *J. Phys.: Conf. Ser.* **123** 012022

[23] Notake T. *et al* 2005 *Plasma Phys. Control. Fusion* **47** 531

[24] Nagasaki K., Ejiri A., Mizuuchi T., Obiki T., Okada H., Sano F., Zushi H., Besshou S., and Kondo K. 1999 *Phys. Plasmas* **6** 556

[25] Ii T. *et al* 2015 *Rev. Sci. Instrum.* **86** 023502

[26] Bornatici M., Cano R., De Barbieri O., and Engelmann F. 1983 *Nucl. Fusion* **23** 1153

[27] Nowak S. and Orefice A. 1993 *Phys. Fluids B* **5** 1945

[28] Poli E., Peeters A. G., and Pereverzev G. V. 2001 *Comp. Phys. Comm.* **136** 90

[29] Balakin A. A., Balakina M. A., and Westerhof E. 2008 *Nucl. Fusion* **48** 065003

[30] Tokuzawa T. *et al* 2010 *Fusion Sci. Technol.* **58** 364

[31] Makino R., Kubo S., Ido T., Shimozuma T., Yoshimura Y., Nishiura M., Igami H., Takahashi H., Ogasawara S., and Mutoh T. 2014 *Proc. 12th Asia Pacific Physics Conference, JPS Conf. Proc.* **1** 015034

[32] Sakakibara S., Yamada H., and LHD Experiment Group 2010 *Fusion Sci. Technol.* **58** 471

[33] Kirov K. K., Leuterer F., Pereverzev G. V., Ryter F., Suttrop W., and ASDEX Upgrade team 2002 *Plasma Phys. Control. Fusion* **44** 2583
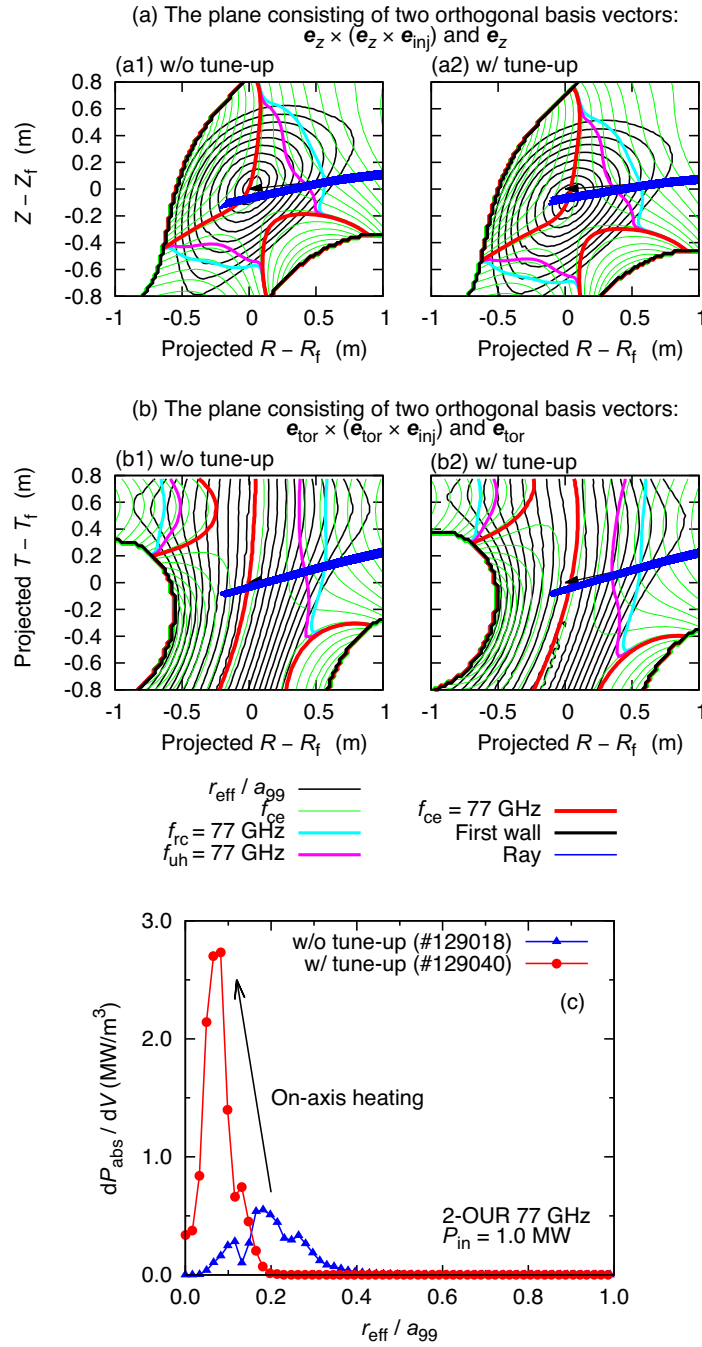
[34] Nagaoka K. *et al* 2015 *Nucl. Fusion* **55** 113020

(a) The plane consisting of two orthogonal basis vectors: $e_z \times (e_z \times e_{inj})$ and e_z

(a1) w/o tune-up

(a2) w/ tune-up

(b) The plane consisting of two orthogonal basis vectors: $e_{tor} \times (e_{tor} \times e_{inj})$ and e_{tor}

(b1) w/o tune-up

(b2) w/ tune-up

r_{eff} / a_{99}

f_{ce}

$f_{rc} = 77$ GHz

$f_{uh} = 77$ GHz

$f_{ce} = 77$ GHz

First wall

Ray

w/o tune-up (#129018)

w/ tune-up (#129040)

(c)

On-axis heating

2-OUR 77 GHz
$P_{in} = 1.0$ MW

Figure 8. Ray-tracing calculation results (1) before and (2) after tuning the injection antenna of the 2-OUR 77 GHz EC beam line for the high temperature plasma under the experimental n_e and T_e profiles along with the 3D equilibrium mapping. Rays are projected on two planes: (a) the plane consisting of two orthogonal basis vectors, $e_z \times (e_z \times e_{inj})$ and e_z, and (b) the plane consisting of two orthogonal basis vectors, $e_{tor} \times (e_{tor} \times e_{inj})$ and e_{tor}, where e_z denotes the unit vector in the vertical direction, e_{tor} denotes the unit vector in the toroidal direction at the 2-O port center, and e_{inj} denotes the unit vector in the direction from the injection antenna center to the target point. Arrowheads denote target points. The contours and lines are plotted as in figure 7. The resultant power deposition profiles as a function of r_{eff}/a_{99} are shown in (c).
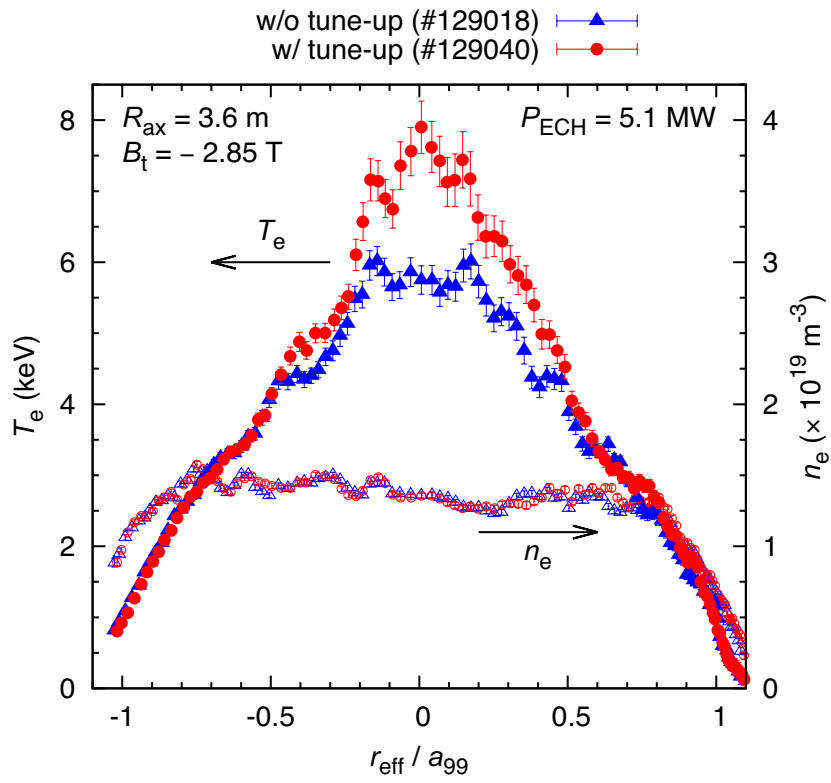
Figure 9. T_e and n_e profiles as a function of r_{eff}/a_{99} before and after tuning the injection antennas for all the EC beam lines.
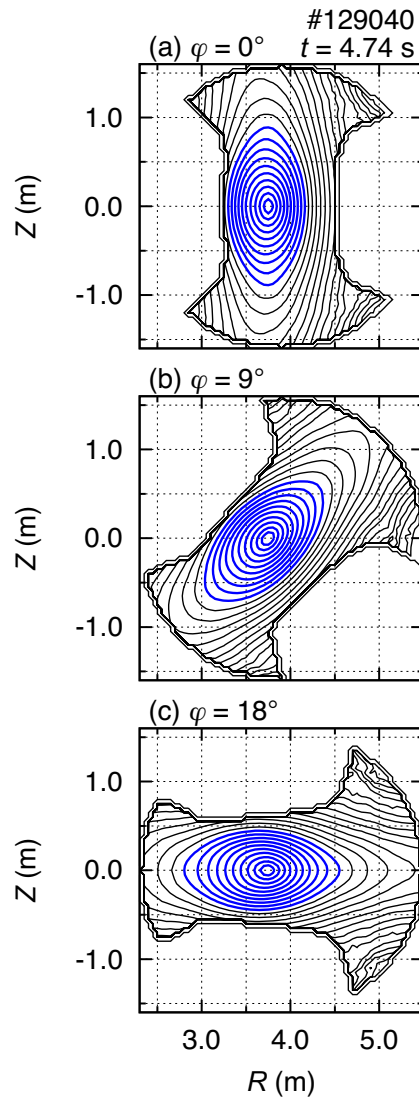
Figure A1. Original (blue color) and extrapolated virtual (black color) magnetic flux surfaces r_{eff}/a_{99} on poloidal planes at (a) $\varphi = 0°$, (b) $\varphi = 9°$, and (c) $\varphi = 18°$. The contour spacing is 0.1.